Journal of Materials Chemistry A

ROYAL SOCIETY OF CHEMISTRY

PAPER

View Article Online
View Journal | View Issue

Cite this: J. Mater. Chem. A, 2024, 12, 2796

Multi-mode mechanoluminescence of fluoride glass ceramics from rigid to flexible media toward multi-scene mechanical sensors†

Yingdan Song,[abc] Jianqiang Xiao,[b] Lei Zhao, *[ac] Zhichao Liu,[b] Yami Ling,[ac] Yingjuan Yan,[ac] Yixuan Xu,[ac] Alexey·Nikolaevich Yakovlev,[d] Tingting Hu,[d] Tatiana Grigorievna Cherkasova,[d] Qiang Xu,*[ac] Canjun Wang*[a] and Xuhui Xu *[b]

The smart mechanical sensing technology based on mechanoluminescence (ML) has potential applications in the fields of wearable mechanical sensors and remote detection of human health due to its characteristics of non-contact, visualization, and remote signal transmission. Herein, a new strategy for multi-mode ML in a rigid and flexible medium by embedding fluoride nanocrystals (CaF_2: Tb^{3+}) in amorphous media was proposed and the intrinsic physical mechanism of energy conversion was clarified. For the rigid transparent CaF_2: Tb^{3+} glass ceramics (GCs), without being fabricated with any special medium, recoverable trap-controlled ML can be generated under friction after X-ray pre-irradiation. Furthermore, the ML composite device fabricated using CaF_2: Tb^{3+} GC powder and flexible stretchable polydimethylsiloxane (PDMS) can achieve self-recovery ML under multimode mechanical stimulation due to the induction of inorganic-organic interface triboelectrification. Finally, rigid accurate stress detection at non-stressed point positions is designed based on the remote transmission of a ML signal owing to the unique optical waveguide effect of GCs, and a flexible mechanical-sensing optical skin for real-time monitoring of human health status is realized by using the CaF_2: Tb^{3+} GC powder/PDMS composite device. This work opens up a new avenue for the realization of multi-scene stress detection based on a rigid/flexible ML material.

Received 14th October 2023
Accepted 14th December 2023

DOI: 10.1039/d3ta06257k

rsc.li/materials-a

1 Introduction

Mechanoluminescence (ML) is a mechanical–optical energy conversion process that occurs under mechanical stimulation, such as compression, stretching, friction, scratching, and impacts, forming a link between luminescence and mechanics,[1–11] which has broad applications in visualization,[12] non-contact mechanical sensing,[13–21] structural health monitoring,[22] artificial intelligence skin,[23–25] and wearable devices.[26,27] Currently, various ML materials have been developed based on the structure composition of the material, mechanical stimulation mode, delocalization/recombination path of the electron–hole pair, fabricating medium of composite devices, and energy conversion modes.[28–31] The macroscopic mechanical–optical energy conversion, which is the essential physical mechanism of ML, is an indirect conversion that comprises two or more microscopic energy conversion processes, such as mechanical-electrical and electrical–optical energy conversion. In the ML generation process, an intermediate physical field, such as piezoelectricity/triboelectricity, serves as a bridge for the conversion of mechanical energy to optical energy.[6] In addition to the structure and performance of the ML material, the intermediate physical field is often closely related to the mechanical stimulation mode and the type of fabricated medium used in ML devices.

Currently, most ML materials can only generate luminescence using ML phosphors and organic elastomers, such as epoxy resin (ER) and polydimethylsiloxane (PDMS), to form composite devices. These organic elastomers can act as a stress conduction medium, transferring the macroscopic mechanical force received by the ML composite device to the luminescent particles and producing an interface interaction with the luminescent particles when subjected to macroscopic mechanical force or deformation, both of which can determine ML generation. For example, piezoelectric crystal-based luminescent particles can generate piezoelectric ML under stress,[1,3] while triboelectric ML can be generated when the triboelectric

[a]School of Physics and Opto-Electronic Technology, Baoji University of Arts and Sciences, Baoji, Shaanxi 721016, P. R. China. E-mail: zhaoleibjwl@163.com; xuqiang@bjwlxy.edu.cn; cjwangbj@126.com

[b]College of Materials Science and Engineering, Kunming University of Science and Technology, Kunming 650093, P. R. China. E-mail: xuxuh07@126.com

[c]Baoji Key Laboratory of Micro-Nano Optoelectronics and Terahertz Technology, Baoji, Shaanxi 721016, P. R. China

[d]T. F. Gorbachev Kuzbass State Technical University, Kemerovo 650000, Russia

† Electronic supplementary information (ESI) available. See DOI: https://doi.org/10.1039/d3ta06257k

potential is induced at the interface between the inorganic luminescent particles and organic elastomer medium.[32–42]

When CaF_2: Tb^{3+} glass ceramics (GCs) were subjected to macroscopic mechanical stimulation as a typical transparent and rigid medium,[43–48] generating obvious elastic deformation related to the direction of the stress application was challenging, except for a small amount of elastic deformation in the specific direction of large area glass. Producing ML in such rigid CaF_2: Tb^{3+} GCs is challenging using the existing ML mechanisms. In our previous study, we found that trap-controlled ML was achieved in $BaLaF_3$: Tb^{3+} GCs after pre-irradiation with a high-energy femtosecond laser, and remote transmission of the ML signal was achieved because of the unique optical waveguide effect of CaF_2: Tb^{3+} GCs, leading to the study of rigid medium ML.[49,50] However, the difference in mechanical properties of the rigid and flexible organic media leads to different application prospects for ML. Thus, studying the same material in rigid and flexible media will further promote the popularization and application of ML in CaF_2: Tb^{3+} GCs.

This work investigates the ML performance of CaF_2: Tb^{3+} GCs in their original rigid and flexible device fabricated with PDMS (Fig. 1a). The rigid CaF_2: Tb^{3+} GCs produce recoverable ML under friction after X-ray pre-irradiation. Furthermore, the CaF_2: Tb^{3+} GCs/PDMS composite device can produce recoverable ML under mechanical stimulation. This study provides a detailed examination of ML characteristics and physical mechanisms in different media, proposes the application of CaF_2: Tb^{3+} GCs in various scenarios, and offers theoretical support for the selection of ML materials for different applications.

2 Experimental section

2.1 Materials and synthesis

A series of glass samples were prepared by using conventional melting-quenching techniques with specific components. The raw materials B_2O_3 (99.99%), SiO_2 (99.99%), ZnO (99.9%), and Na_2CO_3 (99.99%) were ground into a powder by using an agate

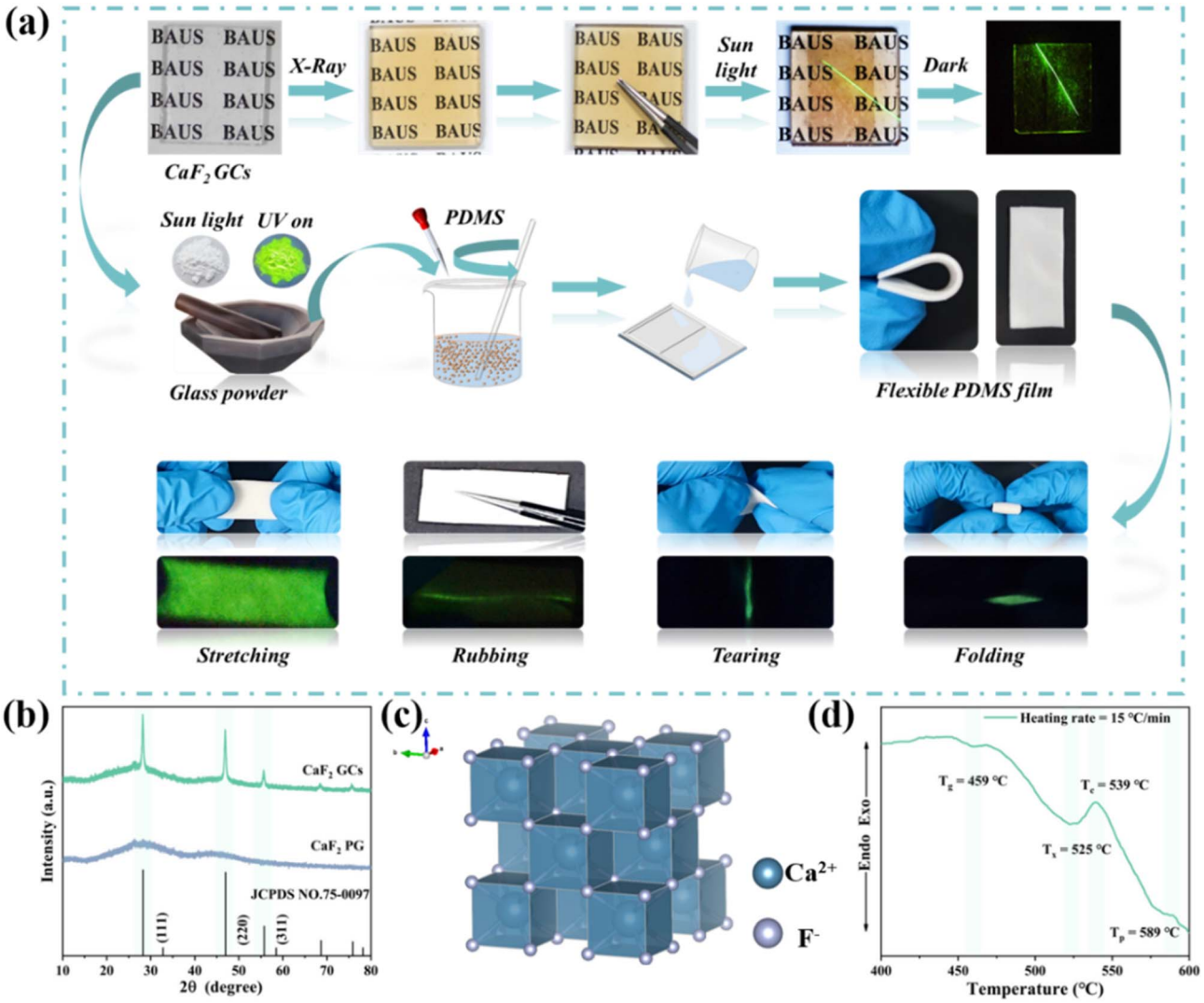

Fig. 1 (a) Schematic diagram of multimode ML based on CaF_2: Tb^{3+} GCs in different media. (b) XRD patterns of PG and CaF_2: Tb^{3+} GCs. (c) Crystal structure of CaF_2. (d) DTA curve of CaF_2: Tb^{3+} GCs.

mortar. All chemical reagents were of analytical grade purity and were purchased from Aladdin Chemical Reagents Ltd. The evenly mixed raw material was then placed in an alumina crucible and melted in air at 1200 °C for 15 min. Furthermore, the melt was poured into a 450 °C preheated copper plate and pressed with another copper plate to form precursor glass (PG). The PG sample was cooled to room temperature (RT) and annealed in a muffle furnace to obtain the CaF_2: Tb^{3+} GCs. Finally, the obtained products were cut and polished for further characterization.

2.2 Preparation of the application device

The flexible film was fabricated by dispersing the CaF_2: Tb^{3+} GC powder in polydimethylsiloxane (PDMS, Sylgard 184, Dow Corning). The ML powder (CaF_2: Tb^{3+} GCs, CaF_2: Eu^{3+} GCs, CaF_2: Eu^{2+} GCs) was mixed well with PDMS (1.5 : 2.5) and then uniformly placed on a mold. The mold with the composite was then placed in an oven and heated at 80 °C for 60 min. Then a flexible ML film was fabricated for the measurement (CaF_2: Tb^{3+} GCs/PDMS, CaF_2: Eu^{3+} GCs/PDMS, CaF_2: Eu^{2+} GCs/PDMS).

2.3 Characterization

An X-ray diffraction (XRD) instrument was operated in the range of 10°–80° at 2θ (Bruk BRUKER D2 PHASER, Germany). The photoluminescence (PL) and photoluminescence excitation (PLE) spectra were recorded with a Hitachi F-7000 fluorescence spectrophotometer with a 150 W Xe lamp as the excitation source. The microstructures of the GCs were analyzed using transmission electron microscopy (TEM) and high-resolution field TEM with a JEM-F200 at 200 kV. Sample morphology was investigated by using a scanning electron microscope (SEM) TESCAN VEGA 3 SEM (Tescan China, Ltd). Energy-dispersive spectrum (EDS) and element mapping were obtained by using energy dispersive spectrometer (Ametek Materials Analysis Division). The differential thermal analysis (DTA) curve was recorded with a heating rate of 15 °C min^{-1} (STA7300, Japan Corporation, Hitachi High-tech Science). The transmission spectrum in the wavelength range of 200–800 nm was recorded by using a Hitachi U-4100 spectrophotometer (Hitachi, Tokyo, Japan). The thermoluminescence (TL) curves were measured by using an FJ-427A pyrometer (Nuclear Instrument Factory, Beijing, China). The electron paramagnetic resonance (EPR) spectrum of the samples was measured by using a Bruker X-band A300-6\1 paramagnetic resonance spectrometer at a frequency of 9.2 GHz at RT. The ML intensity was characterized by using an MS-T3001 friction and wear testing machine, a multi-mode force-luminescence detection system (Qingdao Qingke Longnuo Environmental Technology Co., Ltd QKLN-ML-2), and the use of an Ocean Insight QE Pro fiber optic spectrometer (FLAME-S-XP1-ES). The distance between the friction interface and the electrostatic measurement probe was fixed at 10 cm, and the wavelength range of the test was from 300–1000 nm. The triboelectric properties were detected through a CSM friction testing machine (Tribometer 3, Switzerland) equipped with an electrostatic measuring probe (SK050, KEYENCE (Japan) Co., Ltd). The distance from the friction interface to the electrostatic measuring probe is fixed at 10 cm, and the CSM friction machine adopts a rotating module with a rotation radius of 3 mm and a speed of 60 rpm. The cathodoluminescence (CL) performance was tested on a modified Mp-Micro-S instrument attached to a SEM. All photographs were captured by using a digital camera (Nikon D7100) at RT.

3 Results and discussion

This work focused on investigating the physical mechanism, energy transfer process, and corresponding luminescence behavior during ML generation in different media with various mechanical stimulations. Fig. 1a depicts the ML phenomenon in different media and the flexible ML composite device fabrication processes. Transparent CaF_2: Tb^{3+} GCs after X-ray pre-irradiation generated recoverable trap-controlled green emitting ML under friction, regardless of the bright and dark environments. By grinding CaF_2: Tb^{3+} GCs (*i.e.*, turning glass into powder) and mixing them with PDMS (CaF_2: Tb^{3+} GCs/PDMS), we designed a self-recovery ML composite device resulting from the triboelectric potential induction of the inorganic-organic mechanical interface. Bright green emitting ML can be observed in the CaF_2: Tb^{3+} GCs/PDMS composite device under different mechanical stimuli, such as compression, friction, stretching, tearing, and folding.

3.1 Phase and structure characterization

As a proof-of-concept experiment, we chose CaF_2: Tb^{3+} GCs as the research material in this work. Fig. 1b and S1 (ESI)† show the X-ray diffraction (XRD) patterns of CaF_2: Tb^{3+} GCs before and after the thermal treatment and the CaF_2: x% Tb^{3+} ($x = 0.1$, 0.3, 0.5, 0.7, and 0.9) samples quenched at 530 °C for 6 h, respectively. These figures demonstrate that heat treatment gradually crystallizes the original amorphous precursor glass (PG) sample, and the precipitated microcrystalline peaks belonging to the (111), (220), and (311) crystal surfaces of the CaF_2 phase are consistent with the standard card (JCPDS NO. 75-0097), indicating that the precipitated microcrystalline phase is CaF_2 and the introduction of Tb^{3+} does not form any impurity phase during the doping process. The transmission electron microscopy (TEM) image of CaF_2: Tb^{3+} GCs in Fig. S2a (ESI)† shows that the microcrystal particles are evenly distributed in the glass matrix. In addition, Fig. S2b (ESI)† shows that the (111) surface average surface spacing of CaF_2: Tb^{3+} GC crystals is 0.3164 nm, and the corresponding fast Fourier transform image verifies the successful precipitation of CaF_2: Tb^{3+} nanocrystals from the amorphous matrix (Fig. S2c ESI†). The scanning electron microscope (SEM) image and energy-dispersive spectrum (EDS) mapping of the GCs (Fig. S3 ESI†) clearly show that the elements are uniformly distributed throughout the sample. The crystal structure diagram of CaF_2 in Fig. 1c shows that F occupies eight sites of the hexahedron and Ca is surrounded by eight F to form a center cube, occupying the Ca sites after doping with Tb. The CaF_2 crystal is a cubic crystal system, with space group $Fm\bar{3}m$ belonging to the cubic system and a centrosymmetric structure. Previous studies revealed that

a crystal with this structure is nonpiezoelectric. Fig. 1d presents the differential thermal analysis (DTA) curve of the sample at a heating rate of 15 °C min^{-1}, which was used to assess the glass characteristics of the annealed samples. The sample exhibits a weak heat absorption tendency at 539 °C, indicating the amorphicity of the sample. The thermal stability (Tc − Tg) is around 80 °C, which is a low value, indicating that the crystallization of the system starts below the crystallization temperature. Thus, according to the peak crystallization temperature of 539 °C, we selected 530 °C as the optimal annealing temperature. Further analysis determined that the glass transition temperature (Tg) is 459 °C, the starting crystallization temperature (Tx) is 525 °C, the peak crystallization temperature (Tc) is 539 °C, and the final crystallization temperature (Tp) is 589 °C.

3.2 ML performance characterization

CaF_2: Tb^{3+} GCs were obtained using the melting and quenching method as well as through heat treatment from a rigid transparent medium. The transmittance of all the CaF_2: Tb^{3+} GCs samples was more than 80% (Fig. S4a ESI†), and the corresponding transmittance and PL characteristics are presented in the ESI† (Fig. S4 ESI†). Because the CaF_2: Tb^{3+} GCs serve as a rigid medium, the physical mechanism of their ML generation is different from that of composite ML devices fabricated in a flexible medium with inorganic phosphors. Thus, the CaF_2: Tb^{3+} GCs were irradiated with X-rays to charge for ML performance characterization. Fig. 2a shows the ML spectrum of the CaF_2: Tb^{3+} GC sample surface under friction pair. The ML spectrum is similar to the PL spectrum originating from Tb^{3+} ions, indicating that only a luminescence center is present.[49] To quantitatively assess the relation between ML intensity and applied loading, Fig. 2b shows the changing relation between ML intensity and applied loading and the linear fitting data, and the insets show ML photos corresponding to various applied loadings. As shown in the photographs, the ML intensity of CaF_2: Tb^{3+} GCs gradually increases with increasing load, and the corresponding ML spectra are presented in Fig. S5a (ESI).† The linear fitting factor is 0.99132 and the friction-induced mechanical-optical response sensitivity is 1.94786. Additionally, a linear relation (Fig. S5c ESI†) was observed between the ML intensity of the CaF_2: Tb^{3+} GCs and the friction speed (Fig. S5b ESI†) under a constant friction load. Fig. 2c shows the ML spectrum before and after the X-ray pre-irradiation of CaF_2: Tb^{3+} GCs. Furthermore, ML is not generated unless the CaF_2: Tb^{3+} GCs are irradiated with X-ray, indicating that X-ray pre-irradiation plays a crucial role in the ML phenomenon of the CaF_2: Tb^{3+} GCs. High-energy ray irradiation of glass materials can cause some point defects within the glass matrix owing to photoionization. Fig. 2d shows the electron paramagnetic resonance (EPR) spectra of the CaF_2: Tb^{3+} GCs before and after X-ray irradiation. The EPR signal ($g = 1.9965$) was observed only after X-ray irradiation, which is attributed to the oxygen-vacancy defects in the glass,[48,55] indicating that the pre-irradiation with X-ray can generate oxygen vacancies within

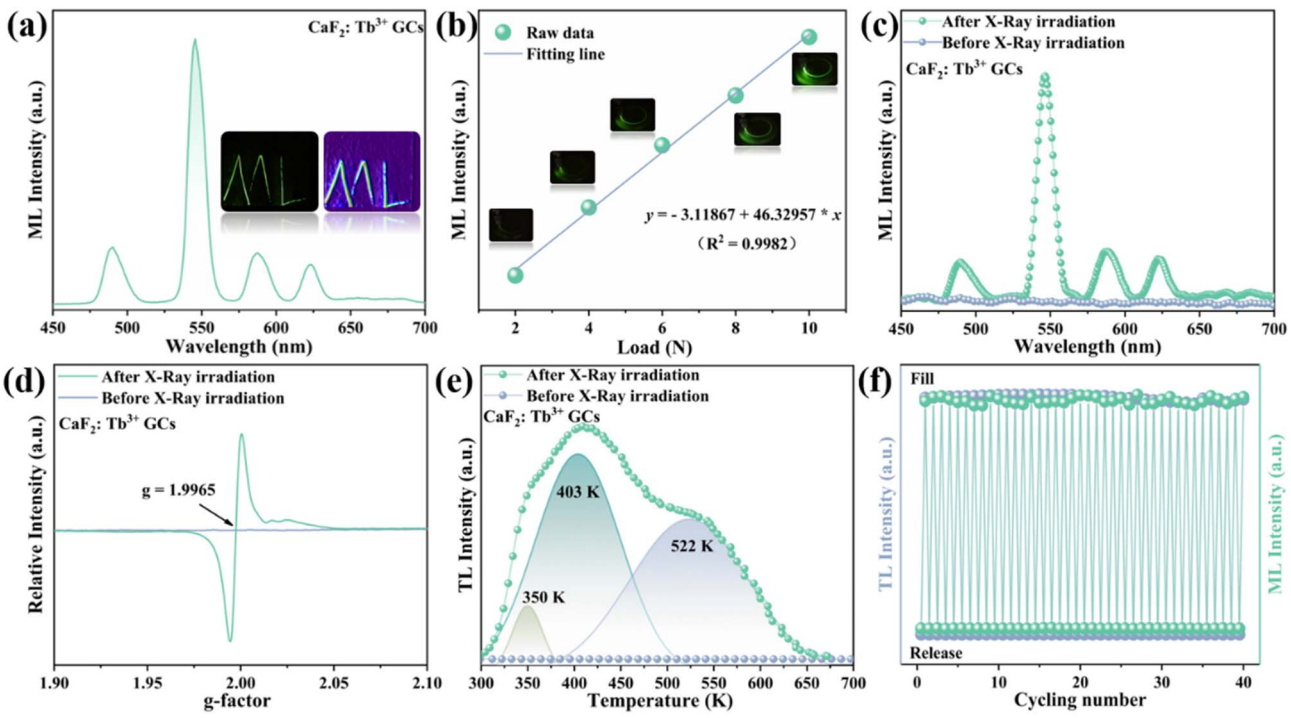

Fig. 2 (a) ML spectrum of the CaF_2: Tb^{3+} GCs (the illustrations show an ML visualization of a handwriting trajectory through long exposure and extracted dimensional color maps from the corresponding photos). (b) The relationship between ML intensity of CaF_2: Tb^{3+} GCs and applied load (insets show the corresponding ML photographs). (c) ML spectra of CaF_2: Tb^{3+} GCs before and after X-ray pre-irradiation. (d) EPR spectra before and after X-ray pre-irradiation of CaF_2: Tb^{3+} GCs. (e) TL curves and Gaussian fitted result of CaF_2: Tb^{3+} GCs before and after X-ray pre-irradiation. (f) Cycling stability of ML/TL in CaF_2: Tb^{3+} GCs.

the CaF_2: Tb^{3+} GC matrix. The TL curves before and after X-ray pre-irradiation are shown in Fig. 2e. A series of continuously distributed traps, trap 1 (350 K), trap 2 (403 K), and trap 3 (522 K), appear after X-ray pre-irradiation which can be fitted using Gaussian fitting. The trap depth E can be estimated from the TL curves using an approximate equation as follows:

$$E = T/500 \text{ (K)} \quad (1)$$

where E is the thermo-active energy of trap depths (eV), which is the energy gap between the electron trap and the conduction band, and T is the TL peak (K).[51–53] The depths of the three traps are 0.7, 0.806, and 1.044 eV, respectively. This result reveals that the oxygen vacancy trap in the CaF_2: Tb^{3+} GCs can effectively capture and store the charge carriers. The TL and ML spectra (Fig. S6a and b ESI†) of the CaF_2: x% Tb^{3+} GCs (x = 0.1, 0.3, 0.5, 0.7, and 0.9) indicate that the TL intensity is quenched at x = 0.7, which is consistent with the PL quenching concentration. Fig. S6c and d (ESI)† show the filling time-dependent TL curves and ML spectra of the CaF_2: Tb^{3+} GCs, respectively. X-Ray irradiation at 40 kV and 30 mA can achieve the upper trap filling limit within 15 min, leading to the maximum TL and ML intensity. Furthermore, the TL after X-ray pre-irradiation follows the same tendency as the ML. This sequence of evidence demonstrates that X-ray pre-irradiation introduced and filled the trap in the glass and the fundamental mechanism of this trap-controlled ML generation is to release the carrier in the trap by mechanical stimulation.

Theoretically, macroscopic mechanical stimulation cannot directly release the carrier for generating ML. Therefore, during ML generation, the macroscopic mechanical energy is first converted into another form of energy that can effectively release the carrier to the strap. Moreover, friction heat is generated when any two media come in contact with one another and undergo friction. Concurrently, the trap-controlled carrier is considerably sensitive to thermal stimulation. Thus, we speculate that the microscopic ML mechanism in the CaF_2: Tb^{3+} GCs is the frictional heat-induced TL. Fig. S7a and b (ESI)† depict the TL curves of the pre-irradiated CaF_2: Tb^{3+} GCs at RT at different times. It can be observed that with the increase in

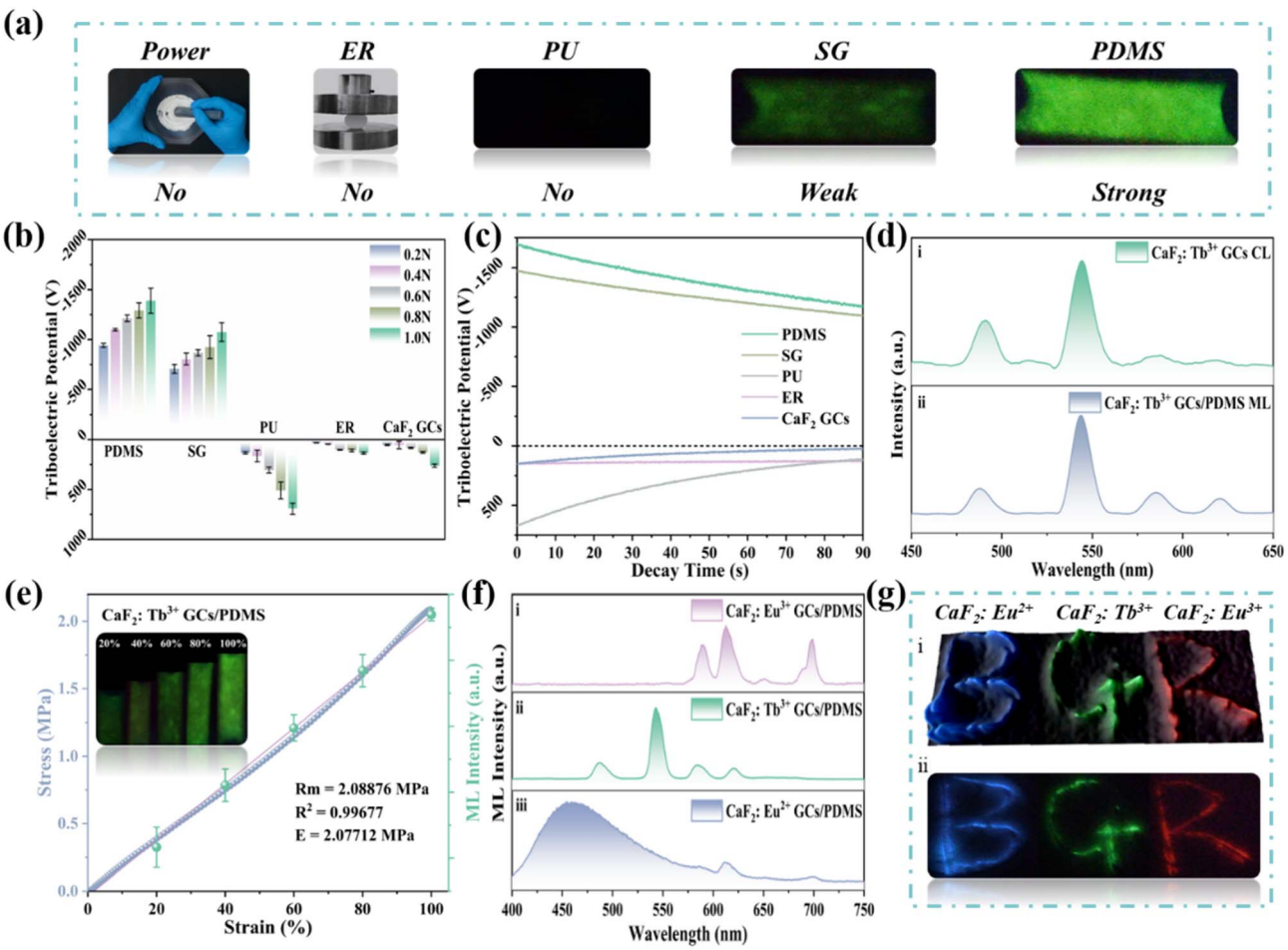

Fig. 3 (a) ML performance of CaF_2: Tb^{3+} GC powder in various media: powder only and with ER, PU, SG, and PDMS. (b) The surface triboelectric potential of polymer matrices when rubbed with CaF_2: Tb^{3+} GC powder for 1 min under different loads. (c) The decay rate of triboelectric potential on polymer surfaces. (d) ML/CL spectra of CaF_2: Tb^{3+} GCs/PDMS elastomers. (e) Stress–strain curves and relationship of ML intensity *versus* strain. (f) ML spectra (from top to bottom) of CaF_2: Eu^{3+} GCs/PDMS, CaF_2: Tb^{3+} GCs/PDMS, and CaF_2: Eu^{2+} GCs/PDMS. (g) ML photos and dimension color maps of CaF_2: Eu^{3+} GCs/PDMS, CaF_2: Tb^{3+} GCs/PDMS, and CaF_2: Eu^{2+} GCs/PDMS.

placement time, the TL intensity gradually reduces because of the effect of RT thermal excitation. After 14 days of placement, the shallow trap retained about 40% of its initial intensity, while the deep trap retained more than 70% of its initial intensity. The variable temperature TL curves (Fig. S7c ESI†) and ML spectra (Fig. S7d ESI†) show that the ML and TL intensity decreases with the increase in temperature, indicating that the ML intensity is directly related to the concentration of charge carriers. Fig. S7e (ESI)† depicts the temperature-dependent TL photographs of the CaF_2: Tb^{3+} GCs after X-ray pre-irradiation for 15 min. It can be seen that the TL of the CaF_2: Tb^{3+} GCs gradually increases with the increasing temperature and slowly decreases above 500 K. This indicates that after X-ray pre-irradiation, thermal stimulation at RT and high temperature can effectively stimulate carrier release in the traps to produce TL. The temperature dependence of the ML is consistent with TL, confirming our speculation about the ML mechanism in the CaF_2: Tb^{3+} GCs. To verify the repeatability of ML in CaF_2: Tb^{3+} GCs under cyclic loading, 40 experiments were performed and the energy was released through repeated charging and heat removal. The sample retained above 95% of the initial intensity (Fig. 2f), confirming that the ML performance of the prepared CaF_2: Tb^{3+} GCs was recoverable. To further demonstrate the ML environmental stability of CaF_2: Tb^{3+} GCs, we tested their ML in water, air, and alcohol every 2 hours for a duration of 24 hours (Fig. S8a–c ESI†). It was observed that the ML stability of CaF_2: Tb^{3+} GC samples was considerably retained. Furthermore, we tested the ML cycling stability of CaF_2: Tb^{3+} GCs and found that the same trends were exhibited over 10 cycles in a 60 s cycle, indicating that the ML performance was stable and repeatable (Fig. S8d ESI†).

Several studies have found that most ML materials do not exhibit ML characteristics alone but the ML phenomenon can be observed after composite encapsulation with an organic flexible medium.[54] Herein, we combined the CaF_2: Tb^{3+} GCs after grinding with various organic matrices to further investigate the effect of the medium on ML performance. As shown in Fig. 3a, no ML was observed during mechanical stimulation (grinding and compression) in the CaF_2: Tb^{3+} GC powder. Furthermore, the composite devices were fabricated with an ER elastomer (CaF_2: Tb^{3+} GCs/ER). When CaF_2: Tb^{3+} GC powder is combined with a flexible matrix, such as polyurethane (PU), silicone (SG), or PDMS (CaF_2: Tb^{3+} GCs/PU, CaF_2: Tb^{3+} GCs/SG, and CaF_2: Tb^{3+} GCs/PDMS), the composite devices can produce large deformations (>50%) at relatively low tensile stress (<5 MPa). As shown in Fig. 3a and S9 (ESI),† under the same strain action, CaF_2: Tb^{3+} GCs/PU exhibited no ML, CaF_2: Tb^{3+} GCs/SG exhibited weak ML, and CaF_2: Tb^{3+} GCs/PDMS exhibited strong ML. To further explain the variability of ML properties of CaF_2: Tb^{3+} GCs in different media, the surface potential of CaF_2: Tb^{3+} GCs, ER, PU, SG, and PDMS after rubbing with CaF_2: Tb^{3+} GCs for 1 min is obtained, as shown in Fig. 3b. It was observed that when CaF_2: Tb^{3+} GCs-CaF_2: Tb^{3+} GCs, ER, and PU as well as CaF_2: Tb^{3+} GCs were rubbed, positive potentials with smaller absolute values were generated. When CaF_2: Tb^{3+} GCs/SG and CaF_2: Tb^{3+} GCs/PDMS are rubbed, the medium obtains electrons with a negative potential, which appears as a negative potential with a large absolute value. Thus, we believe that the absence of ML after CaF_2: Tb^{3+} GCs/ER and CaF_2: Tb^{3+} GCs/PU is because of insufficient triboelectric potential generated by ER and PU friction to reach the minimum threshold for ML generation. However, owing to the large triboelectric potential

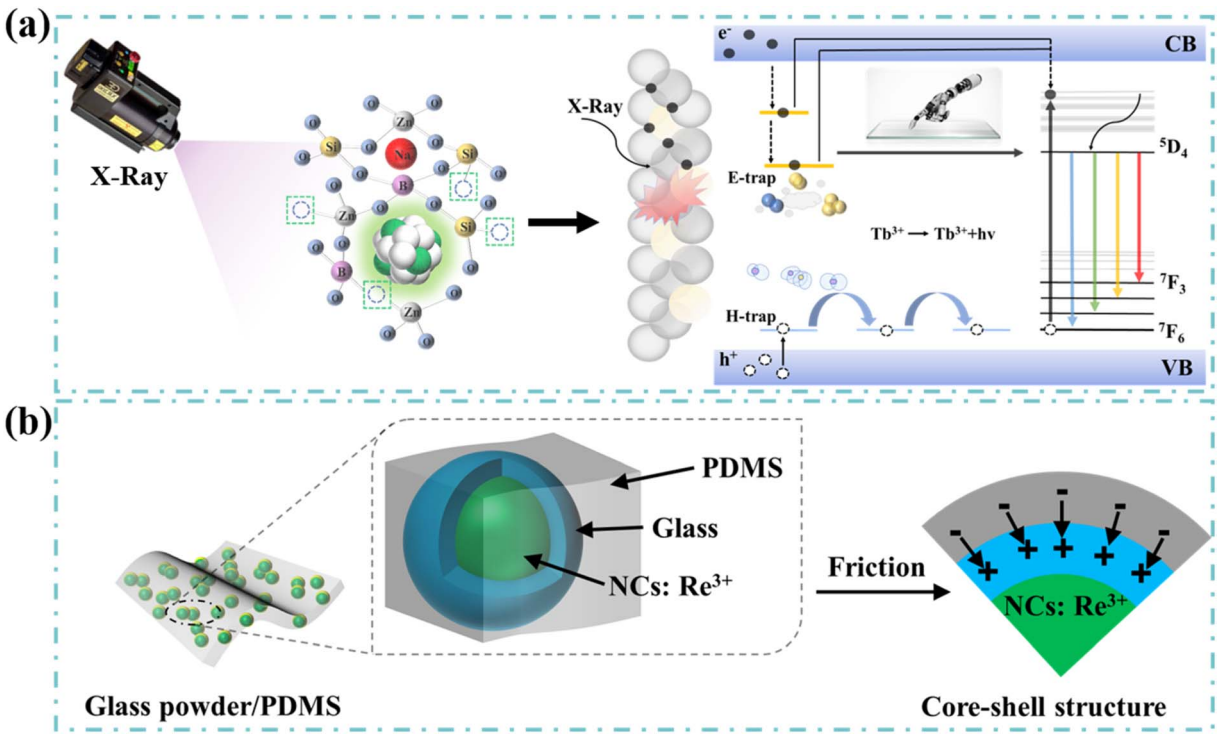

Fig. 4 (a) Mechanism diagram of the ML in CaF_2: Tb^{3+} GCs. (b) Mechanism diagram of the ML in the CaF_2: Tb^{3+} GCs/PDMS flexible device.

generated during the contact separation process of the inorganic–organic mechanical interface in CaF_2: Tb^{3+} GCs/SG and CaF_2: Tb^{3+} GCs/PDMS, ML can directly stimulate ML particles. Additionally, the charge decay curve in Fig. 3c well explains the different ML intensities between CaF_2: Tb^{3+} GCs/SG and CaF_2: Tb^{3+} GCs/PDMS. While the luminescence behavior of the ML process is similar to that of CL in the electron–hole pair delocalization/recombination path, the CL spectrum of CaF_2: Tb^{3+} GCs/PDMS, as given in Fig. 3d, agrees with the ML spectrum.[38] The results suggest that the ML mechanism of CaF_2: Tb^{3+} GCs/SG and CaF_2: Tb^{3+} GCs/PDMS is a direct excitation-emission process induced by the interface triboelectric field. Furthermore, the proposed ML excitation pathway of electron bombardment under a triboelectric field is also deemed reasonable. Hence, we believe that the ML mechanism of CaF_2: Tb^{3+} GCs/SG and CaF_2: Tb^{3+} GCs/PDMS conforms to the interface friction-induced electron bombardment model of direct excitation-emission. Furthermore, the separation of ML particles from the polymer chain weakens the interfacial binding of the composite elastomer, causing a decrease in the interface triboelectric field and the interface friction intensity. Fig. 3e shows the stress–strain curves of the CaF_2: Tb^{3+} GCs/PDMS composite elastomer tested on a tensile test machine, with an elastic modulus and tensile intensity of 2.07712 and 2.08876 MPa, respectively. The ML intensity and stress variables exhibit a linear relation. The inset is an ML photograph of CaF_2: Tb^{3+} GCs/PDMS during the tensile mechanical action of different shape variables. The intensity of ML gradually increases with the increase in strain. Moreover, to demonstrate the universality of this ML mechanism in a flexible medium, we also studied the ML characteristics of CaF_2: Tb^{3+} GCs/PDMS, CaF_2: Eu^{3+} GCs/PDMS, and CaF_2: Eu^{2+} GCs/PDMS. The results reveal that the tri-color (red: CaF_2: Eu^{3+} GCs/PDMS, green: CaF_2: Tb^{3+} GCs/PDMS, and blue: CaF_2: Eu^{2+} GCs/PDMS) ML of a single matrix is achieved in the material, displaying the ML spectrum of CaF_2: Eu^{3+} GCs/PDMS, CaF_2: Tb^{3+} GCs/PDMS, and CaF_2: Eu^{2+} GCs/PDMS samples (Fig. 3f), as well as the corresponding ML visualization of handwritten traces extracted from dimension-color maps *via* long exposure (Fig. 3g). The photos exhibit tri-color ML (Fig. 3g(ii)), while the dimensional color diagram

Fig. 5 (a) Diagram of potential application of CaF_2: Tb^{3+} GCs. (b) Diagram of potential application of CaF_2: Tb^{3+} GCs/PDMS.

(Fig. 3g(i)) indicates that it can exhibit ML intensity distribution.

3.3 ML mechanism analysis

The mechanisms of ML generation in CaF_2: Tb^{3+} GCs differ in rigid and flexible media, which is primarily attributed to the variation in mechanical properties of the medium, mechanical stimulation mode, and the interaction between ML particles and the medium. First, as shown in Fig. 4a, the ML of a rigid CaF_2: Tb^{3+} GC medium is primarily caused by TL induced *via* friction heat generation, and the microscopic energy conversion process is primarily the gradual conversion of mechanical energy to thermal energy and then to optical energy. The amorphous glass network structural matrix contains numerous bridging oxygen bonds, and a large number of oxygen-vacancy traps are very easily formed under X-ray pre-irradiation, which will become an effective trap center. X-Ray irradiation effectively promotes the filling of the carriers in the trap. When the object (such as the friction pair) comes into contact with the ML CaF_2: Tb^{3+} GCs and produces relative movement, the mechanical energy generated by the friction force is converted into Joule heat to produce TL. During this, the macroscopic phenomenon presented in this instantaneous process is the ML under the action of friction. The increase in ML intensity with friction load and friction rate is attributed to the fact that the work done by the friction force increases with the load and rate, producing more Joule heat. The reproducible pre-irradiation and release of carriers in traps is the fundamental cause of recoverable trap-controlled ML.

The self-recovery ML generated by CaF_2: Tb^{3+} GCs/PDMS can be attributed to the induction of electron bombardment because of friction potential at the inorganic–organic mechanical interface, as shown in Fig. 4b. When subjected to multi-mode mechanical stimulation (such as stretching and friction), an interfacial triboelectric field between the CaF_2: Tb^{3+} GC particles and the SG or PDMS polymer chains is generated due to interfacial friction. This electric field interaction can cause excitation from the valence band to the conduction band (CB), followed by ML emission after the electrons in the CB are transferred to the Tb^{3+} excited state level and recombine with the holes in the ground state. The generation of ML in a flexible medium is primarily derived from the energy conversion of mechanical energy to electric energy and then to optical energy.

3.4 Potential application of ML devices

Based on the advantages of two different media, we have designed two different types of applications for CaF_2: Tb^{3+} GC glass fibers and plate glass. First, based on the glass optical waveguide effect, as shown in Fig. 5a, we observed a change in the intensity of the waveguide with distance and force in glass fibers and plate glass. This effect can be used to monitor stress points and stress values at the edges of glass in structures such as railways, bridges, windows, and aircraft, and for structural health monitoring. We can transmit the monitoring results to a computer *via* a Wi-Fi signal to achieve remote stress detection as shown in Fig. 5a. Secondly, we have also prepared CaF_2: Tb^{3+} GCs/PDMS elastomers for optical skin. The elastomer can detect mechanical data from various joints of athletes, monitor and analyze their exercise habits, and provide visual and mechanical feedback, thereby providing data support for analyzing the physical condition of athletes as shown in Fig. 5b.

4 Conclusion

In summary, the CaF_2: Tb^{3+} GCs are synthesized using the melt-quenching method. X-Ray pre-irradiation is employed to form numerous hypoxic centers in the amorphous structure of CaF_2: Tb^{3+} GCs, serving as effective trap centers. These trap centers facilitated the transfer of carriers to the emitting center, resulting in the production of bright green ML in a rigid transparent mass. The atomic contact between CaF_2 NCs and the amorphous structure played a crucial role in promoting efficient energy transfer between the trap and the emitting center. The application of force induced the carriers in the trap to transfer to the emitting center, leading to ML generation. Furthermore, the ground CaF_2: Tb^{3+} GC powder mixed with PDMS produced flexible films that exhibited bright green ML due to direct excitation of the center through contact between the powder particles and colloids. This study achieved the first realization of rigid/flexible multi-scenario ML using the same material through trap-controlled and triboelectrification for direct excitation of two different ML mechanisms. Additionally, tri-color ML is accomplished by incorporating Eu^{2+}, Tb^{3+}, and Eu^{3+}, enabling the potential use of full-spectrum stress displays. By considering the disparity between rigid and flexible media, precise detection devices for determining the stress-free point position and real-time monitoring of athletes' exercise states are designed separately. This comprehensive and in-depth study encompasses the mechanisms and applications of ML, providing valuable guidance for future research on ML materials in the field of rigid/flexible multi-scene.

Consent

I declare that I am the patient whose information is included in the manuscript entitled “Multi-mode mechanoluminescence of fluoride glass ceramics from rigid to flexible media toward multi-scene mechanical sensors”. I understand that the manuscript will be published and that my personal and medical information may be disclosed, and I hereby give my consent for the publication of this information. I have been informed of the purpose of the manuscript and the type of information that will be included. I am aware that my identification will be kept confidential and that my personal information will only be used for research purposes. I understand that my participation in this research is voluntary, and I am free to withdraw my consent at any time. I have been provided with an opportunity to ask any questions regarding my participation, and all my questions have been answered. I further understand that my withdrawal of consent will not affect the quality or outcome of the research. I understand that my consent is necessary for publication, and I consent to the publication of my personal and medical information in the manuscript.

Author contributions

Yingdan Song: conceptualization, investigation, validation, visualization, writing – original draft, supervision. Jianqiang Xiao: conceptualization, investigation, validation, visualization, supervision. Lei Zhao: conceptualization, supervision, writing – review & editing, funding acquisition. Zhichao Liu: writing – review & editing. Yami Ling: investigation, supervision, validation. Yingjuan Yan: investigation. Yixuan Xu: investigation. Alexey·Nikolaevich Yakovlev: investigation. Tingting Hu: investigation. Tatiana Grigorievna Cherkasova: investigation. Qiang Xu: funding acquisition. Canjun Wang: methodology. Xuhui Xu: conceptualization, supervision, writing – review & editing, funding acquisition. All authors contributed to data analysis, discussions, and manuscript preparation. All authors have given approval to the final version of the manuscript.

Conflicts of interest

There are no conflicts of interest to declare.

Acknowledgements

This work was supported by the International Science and Technology Cooperation and Exchanges Project of Shaanxi (Project No. 2021KW-39), the Scientific Research Program Funded by the Shanxi Provincial Education Department (Project No. 22JC002), the Key Science and Technology Program of Shaanxi Province (Project No. 2023-YBGY-370), the Scientific Research Program Funded by the Shaanxi Provincial Education Department (Grant No. 22JK0245), and the Yunnan Major Scientific and Technological Projects (Grant No. 202202AG050004 and 202202AG050016).

References

1 Z. Huang, B. Chen, B. Ren, D. Tu, Z. Wang, C. Wang, Y. Zheng, X. Li, D. Wang, Z. Ren, S. Qu, Z. Chen, C. Xu, Y. Fu and D. Peng, Smart Mechanoluminescent Phosphors: A Review of Strontium-Aluminate-Based Materials, Properties, and Their Advanced Application Technologies, *Adv. Sci.*, 2023, **10**, e2204925.

2 P. Xiong, M. Peng and Z. Yang, Near-infrared mechanoluminescence crystals: a review, *iSCI*, 2020, **24**(1), 101944.

3 J.-C. Zhang, X. Wang, G. Marriott and C.-N. Xu, Trap-controlled mechanoluminescent materials, *Prog. Mater. Sci.*, 2019, **103**, 678–742.

4 S. Wu, B. Xiao, Y. Xiao, P. Shao, Y. Wang and P. Xiong, Cr3+-activated broadband near-infrared mechanoluminescence in garnet compound, *Nano Energy*, 2023, **116**, 108811.

5 A. Qasem, P. Xiong, Z. Ma, M. Peng and Z. Yang, Recent Advances in Mechanoluminescence of Doped Zinc Sulfides, *Laser Photonics Rev.*, 2021, **15**, 2100276.

6 Y. Du, Y. Jiang, T. Sun, J. Zhao, B. Huang, D. Peng and F. Wang, Mechanically Excited Multicolor Luminescence in Lanthanide Ions, *Adv. Mater.*, 2019, **31**, e1807062.

7 S. M. Jeong, S. Song, S. K. Lee and N. Y. Ha, Color manipulation of mechanoluminescence from stress-activated composite films, *Adv. Mater.*, 2013, **25**, 6194–6200.

8 J. C. Zhang, N. Gao, L. Li, S. Wang, X. Shi, M. Sun, X. Yan, H. W. He, X. Ning, B. Huang and J. Qiu, Discovering and Dissecting Mechanically Excited Luminescence of Mn2+ Activators via Matrix Microstructure Evolution, *Adv. Funct. Mater.*, 2021, **31**, 2100221.

9 Y. Xiao, P. Xiong, S. Zhang, Y. Sun, N. Yan, Z. Wang, Q. Chen, P. Shao, M. G. Brik, S. Ye, D. Chen and Z. Yang, Cation-defect-induced self-reduction towards efficient mechanoluminescence in Mn2+-activated perovskites, *Mater. Horiz.*, 2023, **10**, 3476–3487.

10 Y. L. Yang, X. C. Yang, J. Y. Yuan, T. Li, Y. T. Fan, L. Wang, Z. Deng, Q. L. Li, D. Y. Wan, J. T. Zhao and Z. J. Zhang, Time-Resolved Bright Red to Cyan Color Tunable Mechanoluminescence from CaZnOS: Bi3+ , Mn2+ for Anti-Counterfeiting Device and Stress Sensor, *Adv. Opt. Mater.*, 2021, **9**, 2100668.

11 Y. Bai, X. Guo, B. Tian, Y. Liang, D. Peng and Z. Wang, Self-Charging Persistent Mechanoluminescence with Mechanics Storage and Visualization Activities, *Adv. Sci.*, 2022, **9**, e2203249.

12 Y. Zhuang, X. Li, F. Lin, C. Chen, Z. Wu, H. Luo, L. Jin and R. J. Xie, Visualizing Dynamic Mechanical Actions with High Sensitivity and High Resolution by Near-Distance Mechanoluminescence Imaging, *Adv. Mater.*, 2022, **34**, e2202864.

13 Y. Zhuang and R. J. Xie, Mechanoluminescence Rebrightening the Prospects of Stress Sensing: A Review, *Adv. Mater.*, 2021, **33**, e2005925.

14 S. Pyo, J. Lee, K. Bae, S. Sim and J. Kim, Recent Progress in Flexible Tactile Sensors for Human-Interactive Systems: From Sensors to Advanced Applications, *Adv. Mater.*, 2021, **33**, e2005902.

15 X. Yang, Y. Cheng, J. Xu, H. Lin and Y. Wang, Stress Sensing by Ratiometric Mechanoluminescence: A Strategy Based on Structural Probe, *Laser Photonics Rev.*, 2022, **16**, 2200365.

16 H. Ji, Y. Tang, B. Shen, X. Qian, Z. Cai, F. Li, M. Su, L. Wu, Y. Ma and Y. Song, Skin-Driven Ultrasensitive Mechanoluminescence Sensor Inspired by Spider Leg Joint Slits, *ACS Appl. Mater. Interfaces*, 2021, **13**, 60689–60696.

17 D. J. Lipomi, M. Vosgueritchian, B. C. Tee, S. L. Hellstrom, J. A. Lee, C. H. Fox and Z. Bao, Skin-like pressure and strain sensors based on transparent elastic films of carbon nanotubes, *Nat. Nanotechnol.*, 2011, **6**, 788–792.

18 N. Li, S. Yu, L. Zhao, P. Zhang, Z. Wang, Z. Wei, W. Chen and X. Xu, Recoverable Dual-Modal Responsive Sensing Materials Based on Mechanoluminescence and Thermally Stimulated Luminescence toward Noncontact Tactile Sensors, *Inorg. Chem.*, 2023, **62**, 2024–2032.

19 H. Z. Wei, D. S. Xu and Q. S. Meng, A Newly Designed Fiber-Optic Based Earth Pressure Transducer with Adjustable Measurement Range, *Sensors*, 2018, **18**, 932.

20 S. Lee, A. Reuveny, J. Reeder, S. Lee, H. Jin, Q. Liu, T. Yokota, T. Sekitani, T. Isoyama, Y. Abe, Z. Suo and T. Someya, A

transparent bending-insensitive pressure sensor, *Nat. Nanotechnol.*, 2016, **11**, 472–478.
21 B. Ren, B. Chen, X. Zhang, H. Wu, Y. Fu and D. Peng, Mechanoluminescent optical fiber sensors for human-computer interaction, *Sci. Bull.*, 2023, 542–545.
22 S. Krishnan, H. Van der Walt, V. Venkatesh and V. B. Sundaresan, Dynamic characterization of elastico-mechanoluminescence towards structural health monitoring, *J. Intell. Mater. Syst. Struct.*, 2017, **28**, 2458–2464.
23 P. Zhang, J. Wu, L. Zhao, Z. Guo, H. Tang, Z. Wang, Z. Liu, W. Chen and X. Xu, Environmentally Stable and Self-Recovery Flexible Composite Mechanical Sensor Based on Mechanoluminescence, *ACS Sustainable Chem. Eng.*, 2023, 4073–4081.
24 X. Tang, W. Yang, S. Yin, G. Tai, M. Su, J. Yang, H. Shi, D. Wei and J. Yang, Controllable Graphene Wrinkle for a High-Performance Flexible Pressure Sensor, *ACS Appl. Mater. Interfaces*, 2021, **13**, 20448–20458.
25 C. Wang, D. Peng and C. Pan, Mechanoluminescence materials for advanced artificial skin, *Sci. Bull.*, 2020, **65**, 1147–1149.
26 S. Chang, Y. Deng, N. Li, L. Wang, C.-X. Shan and L. Dong, Continuous synthesis of ultra-fine fiber for wearable mechanoluminescent textile, *Nano Res.*, 2023, 9379–9386.
27 D. Lu, T. Liu, X. Meng, B. Luo, J. Yuan, Y. Liu, S. Zhang, C. Cai, C. Gao, J. Wang, S. Wang and S. Nie, Wearable Triboelectric Visual Sensors for Tactile Perception, *Adv. Mater.*, 2023, **35**, e2209117.
28 H. Deng, Z. Yang, G. Li, D. Ma, Z. Xie, W. Li, Z. Mao, J. Zhao, Z. Yang, Y. Zhang and Z. Chi, Dynamic organic mechanoluminescence (ML): The roles of Mechano-induced conformational isomer and energy transfer from ML to photoluminescence (PL), *Chem. Eng. J.*, 2022, **438**, 135519.
29 R. A. D. M. Ranasinghe, Y. Tanaka, M. Okuya, M. Shimomura and K. Murakami, Structural characterizations of organic-based materials with extensive mechanoluminescence properties, *J. Lumin.*, 2017, **190**, 413–423.
30 Y. Zhao, D. Peng, G. Bai, Y. Huang, S. Xu and J. Hao, Multiresponsive Emissions in Luminescent Ions Doped Quaternary Piezophotonic Materials for Mechanical-to-Optical Energy Conversion and Sensing Applications, *Adv. Funct. Mater.*, 2021, **31**, 2010265.
31 Y. L. Zhong, S. N. Basu and Z. Sun, Nanomaterials and Composites for Energy Conversion and Storage, *Jom*, 2021, **73**, 2752–2753.
32 W. Wang, Z. Wang, J. Zhang, J. Zhou, W. Dong and Y. Wang, Contact electrification induced mechanoluminescence, *Nano Energy*, 2022, **94**, 106920.
33 Y. Xie and Z. Li, Triboluminescence: Recalling Interest and New Aspects, *Chem*, 2018, **4**, 943–971.
34 Z. L. Wang and A. C. Wang, On the origin of contact-electrification, *Mater. Today*, 2019, **30**, 34–51.
35 H. Zou, L. Guo, H. Xue, Y. Zhang, X. Shen, X. Liu, P. Wang, X. He, G. Dai, P. Jiang, H. Zheng, B. Zhang, C. Xu and Z. L. Wang, Quantifying and understanding the triboelectric series of inorganic non-metallic materials, *Nat. Commun.*, 2020, **11**, 2093.
36 S. Lin, L. Xu, C. Xu, X. Chen, A. C. Wang, B. Zhang, P. Lin, Y. Yang, H. Zhao and Z. L. Wang, Electron Transfer in Nanoscale Contact Electrification: Effect of Temperature in the Metal-Dielectric Case, *Adv. Mater.*, 2019, **31**, e1808197.
37 S. Lin, C. Xu, L. Xu and Z. L. Wang, The Overlapped Electron-Cloud Model for Electron Transfer in Contact Electrification, *Adv. Funct. Mater.*, 2020, **30**, 1901418.
38 S. Lin, L. Xu, L. Zhu, X. Chen and Z. L. Wang, Electron Transfer in Nanoscale Contact Electrification: Photon Excitation Effect, *Adv. Mater.*, 2019, **31**, e1901418.
39 X. Y. Wei, X. Wang, S. Y. Kuang, L. Su, H. Y. Li, Y. Wang, C. Pan, Z. L. Wang and G. Zhu, Dynamic Triboelectrification-Induced Electroluminescence and its Use in Visualized Sensing, *Adv. Mater.*, 2016, **28**, 6656–6664.
40 H. Zou, Y. Zhang, L. Guo, P. Wang, X. He, G. Dai, H. Zheng, C. Chen, A. C. Wang, C. Xu and Z. L. Wang, Quantifying the triboelectric series, *Nat. Commun.*, 2019, **10**, 1427.
41 X. Y. Wei, L. Liu, H. L. Wang, S. Y. Kuang, X. Zhu, Z. L. Wang, Y. Zhang and G. Zhu, High-Intensity Triboelectrification-Induced Electroluminescence by Microsized Contacts for Self-Powered Display and Illumination, *Adv. Mater. Interfaces*, 2018, **5**, 1701063.
42 Y. Bai, F. Wang, L. Zhang, D. Wang, Y. Liang, S. Yang and Z. Wang, Interfacial triboelectrification-modulated self-recoverable and thermally stable mechanoluminescence in mixed-anion compounds, *Nano Energy*, 2022, **96**, 107075.
43 Z. Cai, S. Kang, X. Huang, X. Song, X. Xiao, J. Qiu and G. Dong, A novel wide temperature range and multi-mode optical thermometer based on bi-functional nanocrystal-doped glass ceramics, *J. Mater. Chem. C*, 2018, **6**, 9932–9940.
44 D. Chen, S. Liu, Z. Wan and Z. Ji, EuF3/Ga2O3 Dual-Phase Nanostructural Glass Ceramics with Eu2+/Cr3+ Dual-Activator Luminescence for Self-Calibrated Optical Thermometry, *J. Phys. Chem. C*, 2016, **120**, 21858–21865.
45 P. Li, M. Peng, L. Wondraczek, Y. Zhao and B. Viana, Red to near infrared ultralong lasting luminescence from Mn2+-doped sodium gallium aluminum germanate glasses and (Al,Ga)-albite glass-ceramics, *J. Mater. Chem. C*, 2015, **3**, 3406–3415.
46 J. Cao, Y. Ding, R. Sajzew, M. Sun, F. Langenhorst and L. Wondraczek, Mechanoluminescence from highly transparent ZGO:Cr spinel glass ceramics, *Opt. Mater. Express*, 2022, **12**, 3238–3247.
47 Z. Feng, J. Zhang, X. Xu, T. Zheng, Y. Guo and J. Lv, Mechanoluminescence properties of Pr3+-doped B2O3-Al2O3-SrO system glass-ceramics, *J. Non-Cryst. Solids*, 2022, **590**, 121676.
48 J. Ueda, A. Hashimoto and S. Tanabe, Orange Persistent Luminescence and Photodarkening Related to Paramagnetic Defects of Nondoped CaO-Ga2O3-GeO2 Glass, *J. Phys. Chem. C*, 2019, **123**, 29946–29953.
49 H. Tang, L. Zhao, Z. Liu, Q. Peng, X. Yu, Q. Wang, F. Zhao, M. Deng, Y. Bai, Z. Wang, T. Wang, J. Qiu and X. Xu, A lanthanide-doped glass-ceramic fiber for stress sensing, *Cell Rep. Phys. Sci.*, 2022, **3**, 101093.

50 L. Yuan, Y. Jin, Y. Su, H. Wu, Y. Hu and S. Yang, Optically Stimulated Luminescence Phosphors: Principles, Applications, and Prospects, *Laser Photonics Rev.*, 2020, **14**, 2000123.
51 K. Huang, X. Dou, Y. Zhang, X. Gao, J. Lin, J. Qu, Y. Li, P. Huang and G. Han, Enhancing Light and X-Ray Charging in Persistent Luminescence Nanocrystals for Orthogonal Afterglow Anti-Counterfeiting, *Adv. Funct. Mater.*, 2021, **31**, 2009920.
52 Z. Wei, W. Chen, Z. Wang, N. Li, P. Zhang, M. Zhang, L. Zhao and Q. Qiang, High-temperature persistent luminescence and visual dual-emitting optical temperature sensing in self-activated CaNb2O6: Tb3+ phosphor, *J. Am. Ceram. Soc.*, 2020, **104**, 1750–1759.
53 Y. Fu, C. Li, F. Zhang, S. Huang, Z. Wu, Y. Wang and Z. Zhang, Site preference and the optical thermometry strategy by different temperature response from two sites environment of Mn2+ in K7ZnSc2B15O30, *Chem. Eng. J.*, 2021, **409**, 128190.
54 J. Wang, K. Yao, K. Cui, J. Zhang, Y. Gu, W. Wang, X. Jin and J. Zhou, Contact Electrification Induced Multicolor Self-Recoverable Mechanoluminescent Elastomer for Wearable Smart Light-Emitting Devices, *Adv. Opt. Mater.*, 2023, 2203112.
55 M. Li, Y. Jin, L. Yuan, B. Wang, H. Wu, Y. Hu and F. Wang, Near-Infrared Long Afterglow in Fe3+-Activated Mg2SnO4 for Self-Sustainable Night Vision, *ACS Appl. Mater. Interfaces*, 2023, **15**, 13186–13194.